galaxies

MDPI

Article

Spectral and Photometric Studies of NGC 3516 in the Optical Range

Saule Shomshekova [1,*], Alexander Serebryanskiy [1], Ludmila Kondratyeva [1], Nazim Huseynov [2], Samira Rahimli [2], Vitaliy Kim [1], Laura Aktay [1] and Yerlan Aimuratov [1]

[1] Fesenkov Astrophysical Institute, Observatory 23, Medeu District, Almaty 050020, Kazakhstan; aserebryanskiy@gmail.com (A.S.); kondratyeva@fai.kz (L.K.); kim@fai.kz (V.K.); aktay@fai.kz (L.A.); aimuratov@fai.kz (Y.A.)

[2] Shamakhy Astrophysical Observatory Named After N. Tusi, Shamakhy District, Y. Mammadaliyev Settlement AZ-5626, Azerbaijan; qaramamedlinazim@gmail.com (N.H.); samira.rahimli.97@gmail.com (S.R.)

* Correspondence: shomshekova.saule@gmail.com

Abstract: This paper presents the results of the photometric and spectral monitoring of the galaxy NGC 3516, which is an active galactic nucleus (AGN) of type Sy 1.5 with a changing look. Observations were carried out at the Fesenkov Astrophysical Institute (FAI, Almaty, Kazakhstan) and the Shamakhy Astrophysical Observatory (ShAO, Shamakhy, Azerbaijan). Spectral monitoring of this galaxy in the wavelength range 4000–7000 Å began in 2020, while photometric observations have been conducted since 2014. During the observation period, estimates of the galaxy's brightness in the *B*, *V* and *Rc* filters were obtained, as well as measurements of the emission line and continuum fluxes. The light curve shows increased brightness of NGC 3516 in 2016 and 2019. The increase of emission line fluxes of Hβ and Hα and continuum began in 2019 and continued until spring 2020, when these characteristics reached their maximal values. A powerful X-ray flare took place on 1 April 2020. A new phase of brightening began in 2021 and has continued until 2025. After reaching their maxima in 2020, the emission fluxes of Hβ and Hα decreased by a factor of 1.5–2 and remained at a low level until 2022–2023, when they began to increase again. Medium-resolution spectra obtained on 20 April 2020, with the 1-meter "West" telescope (TSHAO) were used to study the broad components of the Hβ and Hα emission line profiles. Model calculations showed that the broad profile of the Hα line consists of a central unshifted component and two (blue and red) components shifted symmetrically relative to the central component by a velocity of $v = 980 \pm 20$ km s^{-1}. The Hβ emission line was relatively weak, so the radial velocity of its components was determined with a large uncertainty: 900 ± 600 km s^{-1}.

Keywords: Seyfert galaxy; spectral observations; photometric observations; light curves; emission lines; broad emission components

check for updates

Academic Editors: Alberto C. Sadun and Jorick S. Vink

Received: 14 February 2025
Revised: 30 April 2025
Accepted: 13 May 2025
Published: 16 May 2025

Citation: Shomshekova, S.; Serebryanskiy, A.; Kondratyeva, L.; Huseynov, N.; Rahimli, S.; Kim, V.; Aktay, L.; Aimuratov, Y. Spectral and Photometric Studies of NGC 3516 in the Optical Range. *Galaxies* **2025**, *13*, 60. https://doi.org/10.3390/galaxies13030060

Copyright: © 2025 by the authors. Licensee MDPI, Basel, Switzerland. This article is an open access article distributed under the terms and conditions of the Creative Commons Attribution (CC BY) license (https://creativecommons.org/licenses/by/4.0/).

1. Introduction

NGC 3516 is a Seyfert galaxy of spectral type Sy 1.5, with spectral variability first detected in 1968 [1,2]. The variability in the Hα line and the first measurement of the time delay of line variations relative to the continuum were first reported in 1973 [3]. NGC 3516 has permitted FeII lines and forbidden [OIII] lines, but they are much narrower compared to those in spectra of typical Sy 1.5 galaxies. In the work by De Rosa et al. (2018) [4], the black hole masses were determined using continuum-Hβ reverberation mapping. In

particular, measurements were obtained for the galaxy NGC 3516, based on observations conducted in January–February 2012 with a cadence of 1 day. The analysis used the fluxes of the broad Hβ emission line and the continuum at λ = 5100 Å. Spectral calibration was performed using the [OIII] emission line. The time lag values measured in 2012 were found to be twice as short, and the continuum luminosity was four times lower compared to the results from 2007 [5]. Spectral features of galaxy NGC 3516 are variable and an increase of coronal lines [6] as well as a strong asymmetry in the profiles of broad lines are observed [7].

NGC 3516 from 1996 to 2018 exhibited clear variability in both the continuum and the broad emission lines [2]. A minimum of activity was recorded in 2014, when the broad lines almost disappeared. This possibly indicates the presence of an obscuring region in NGC 3516 and is supported by absorption in the ultraviolet and X-ray [8–10]. The profiles of the broad Hα and Hβ lines in NGC 3516 show a complex structure with features in the wings of the line profiles and an enhanced peak, indicating the complexity of the Broad Line Region (BLR). The time delays between changes in the continuum and the broad emission lines allowed the estimation of the central black hole mass, $(4.73 \pm 1.40) \times 10^7\ M_{\odot}$, which is consistent with previous calculations [4,11].

Popovic et al. (2023) [7] discovered a very complex structure of the BLR during the active phase of NGC 3516 by looking at broad and strong emission lines. There is a distinct disk-like BLR that contributes to the enhancement of the flux in the wings of the broad lines, as well as an additional Intermediate Line Region (ILR) that enhances the intensity in the core of the line. During the high-activity phase, the ILR emission is located near the center of the line, although in some cases, it is slightly red-shifted. In the low-activity phase (i.e., type 2 phase), the ILR component is significantly blue-shifted, indicating gas outflow.

To analyze the variability of the broad emission line components as manifestations of dynamic processes in the inner regions of NGC 3516, we relied on previous studies by various researchers in this field. For the first time, the mass of the massive central body of the galaxy was estimated using echo mapping based on the measurement of the BLR size [12]. Urry and Padovani (1995) [13] used continuous temporal photometric data and spectral observations to determine the parameters of the BLR.

Despite numerous studies, the nature of the variability of NGC 3516 remains not fully understood. The main proposed scenarios include obscuration by dust along the line of sight [14] and intrinsic changes in the accretion disk. The present work provides new observational data that may be useful for further analysis.

2. Observatories, Telescopes and Equipment

The presented study used observational data obtained at Fesenkov Astrophysical Institute (Kazakhstan) and Nasreddin Tusi Shamakhy Astrophysical Observatory (Azerbaijan). Several instruments were employed for conducting photometric and spectral observations. The description and characteristics of the instruments used are presented in Table 1.

Table 1. Characteristics of observational instruments.

Telescope [1]	Detector	Gratings	Tasks	Field of View	Location [2]
"East" Zeiss-1000	CCD Apogee Alta U9000, *BVRc* filters	–	Photometry	19′ × 19′	TSHAO
"West" Zeiss-1000	CCD Apogee Alta U16M D9	300–2400 L/mm	Spectroscopy	19′ × 19′	TSHAO
Zeiss-2000	Andor, 2048 × 2048, 1 pix = 13.5 µm	UAGS, F = 200 mm, f/2, D = 146 Å/mm	Spectroscopy	15′ × 15′	SHAO

[1] "East" Zeiss-1000: D = 1050 mm, F = 6700 mm; "West" Zeiss-1000: D = 1000 mm, F = 7800 mm; Zeiss-2000: D = 2000 mm, F = 3600 mm. [2] TSHAO: Tien-Shan Astronomical Observatory, Kazakhstan; SHAO: Shamakhy Astrophysical Observatory, Azerbaijan.

2.1. Methodology of Photometric Analysis

During the photometric observations, images of the object were obtained sequentially in the *B*, *V* and *Rc* filters with a time interval of approximately 10 s. Then, a new *B*, *V*, *Rc* image series started again. The time interval between the start of the 1st, 2nd and subsequent series was about 1–2 min, depending on the exposure duration. The acquired frames were then corrected using calibration files: dark and flat. Standard stars with known *B*, *V* and *Rc* magnitudes were selected within the frame near the object. Therefore, atmospheric extinction does not affect the results. Brightness measurements were performed using the MaximDL Pro V6 [15] software suite. For a measure of images of galaxy NGC 3516, an aperture of $6''$ was used. The star GSC 04391−00762 with coordinates RA: 11^h:06^m:29^s, Dec: $+72^\circ$:35^m:49^s and known brightness values $B = 13.921$, $V = 13.403$, $Rc = 13.074$ [16] was chosen as the photometric standard. To convert instrumental magnitudes to the standard *B*, *V* and *Rc* system, the corresponding systems of equations were applied [17]. Uncertainties of the photometric values depend on the signal-to-noise ratio, calibration accuracy and atmospheric conditions and do not exceed 0.01 mag.

2.2. Methodology of Spectral Analysis

The data obtained from SHAO and FAI from 2020 to 2023 were used for the spectral analysis. The spectral data were fully reduced using the IRAF version 2.16 [18] software package. The reduction process included dark frame subtraction, wavelength calibration using a He–Ne–Ar lamp and one-dimensional spectrum extraction from the two-dimensional spectral images. An aperture extraction window ranging from 5 to 13 pixels was applied, depending on seeing conditions and signal-to-noise ratio. Flux calibration was performed using standard spectrophotometric stars [19], and atmospheric absorption was taken into account. To correct for absorption within our galaxy, the value of $E(B-V)$ was taken from the NASA/IPAC Extragalactic Database (NED),[1] based on the dust extinction maps by Schlafly and Finkbeiner [20]. Due to the low redshift of the object ($z \approx 0.009$), no additional correction for intergalactic absorption was applied. The final data also underwent absolute flux calibration and redshift correction, allowing for accurate measurement of emission line fluxes. In our work, we used the approximation of the broad components of Hα and Hβ with the composite models, applying `Gaussian` and `Voigt` functions to describe the line profile shapes. Bayesian analysis and the Bayesian factor (see Appendix A) were utilized for selecting the most likely model. The nested sampling method was used to reach the models' reliability and posterior distributions of the parameters, implemented in the `DYNESTY` package [21,22]. Non-informative uniform distributions were chosen as prior information for the parameters.

3. Results

3.1. Results of Photometric and Spectral Studies of the Galaxy NGC 3516

The light curve in Figure 1 presents the results of the measurements obtained between 2014 and 2025 and supplemented by the results from [2,6]. The errors of *B*, *V*, and *Rc* magnitudes do not exceed 0.01 mag.

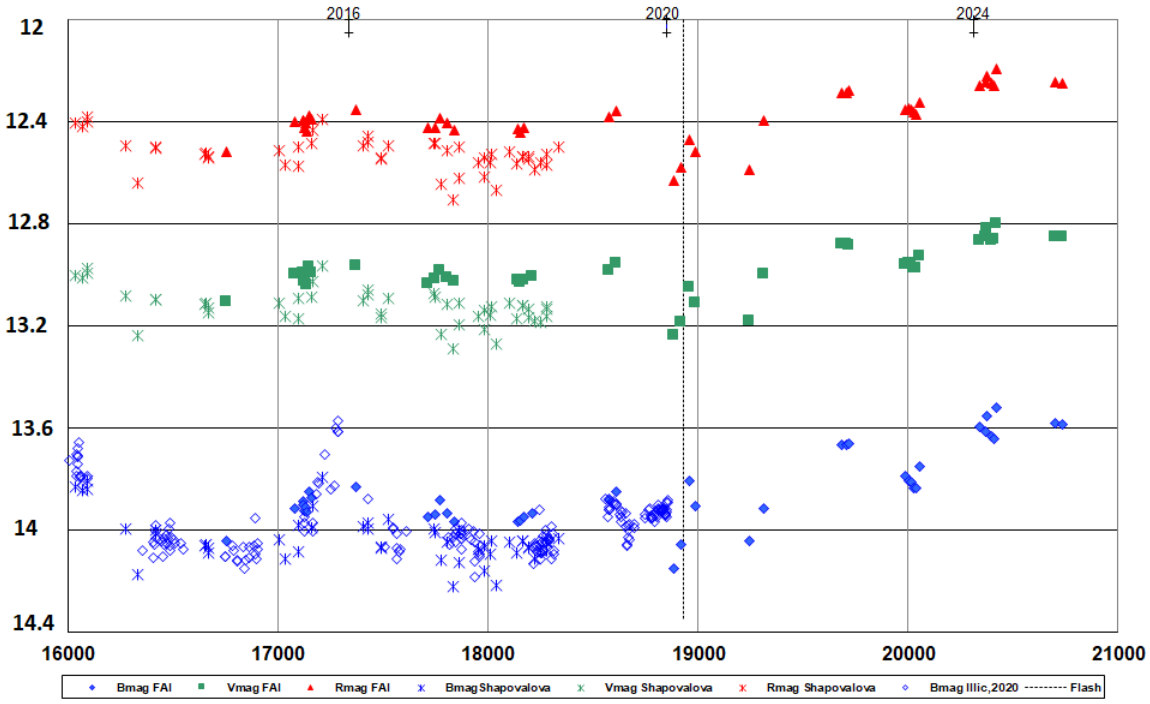


Figure 1. Light curves of NGC 3516 in B (blue), V (green), Rc (red) filters in 2014–2025. On the X-axis: Julian Date−2,440,000; on the Y-axis: apparent stellar magnitude. Empty squares denote data from [6], crosses denote data from [2], other points are FAI data. The vertical dotted line corresponds to the moment of reaching the maximum of the X-ray flare, published in [6,23,24].

The brightness of NGC 3516 fluctuated during 2019–2022 with the following amplitudes: $\Delta B = 0.35$ mag, $\Delta V = 0.2$ mag, $\Delta Rc = 0.3$ mag. During the outburst, the X-ray flux peaked on 1 April 2020, showing the highest value recorded for NGC 3516 by the Neil Gehrels Swift Observatory [24]. According to our observations and the data presented in Figure 1, the optical brightness of the galaxy (in B, V and Rc filters) began to increase in April 2020, shortly after the peak in the X-ray domain recorded on 1 April 2020. We note that the onset of the optical flare (18 April 2020) occurs with a characteristic delay relative to the X-ray maximum, which is consistent with the results reported by other authors [24]. At this stage, as seen in the plot, there is a rise in optical brightness up to 0.2 mag in Rc and 0.1–0.15 mag in B and V. However, immediately following the onset of this flare, a temporary drop in brightness of approximately 0.1 mag is observed. Thus, the described pattern represents a complex brightness evolution, including both a rising phase and local fluctuations, which is typical for active nuclei of Seyfert galaxies.

We analyzed the color variability of the object by plotting the dependence of $(B - V)$ and $(V - Rc)$ on the brightness in the V filter (see Figure 2). The plot shows a clear trend of decreasing $(B - V)$ with increasing brightness in the V filter, indicating the presence of a "bluer when brighter" (BWB) effect. This is characteristic of active galactic nuclei and indicates that the object becomes bluer as the brightness increases. At the same time, $(V - Rc)$ remains almost constant over the entire brightness interval, which confirms that the main contribution to the color change comes from the blue range.

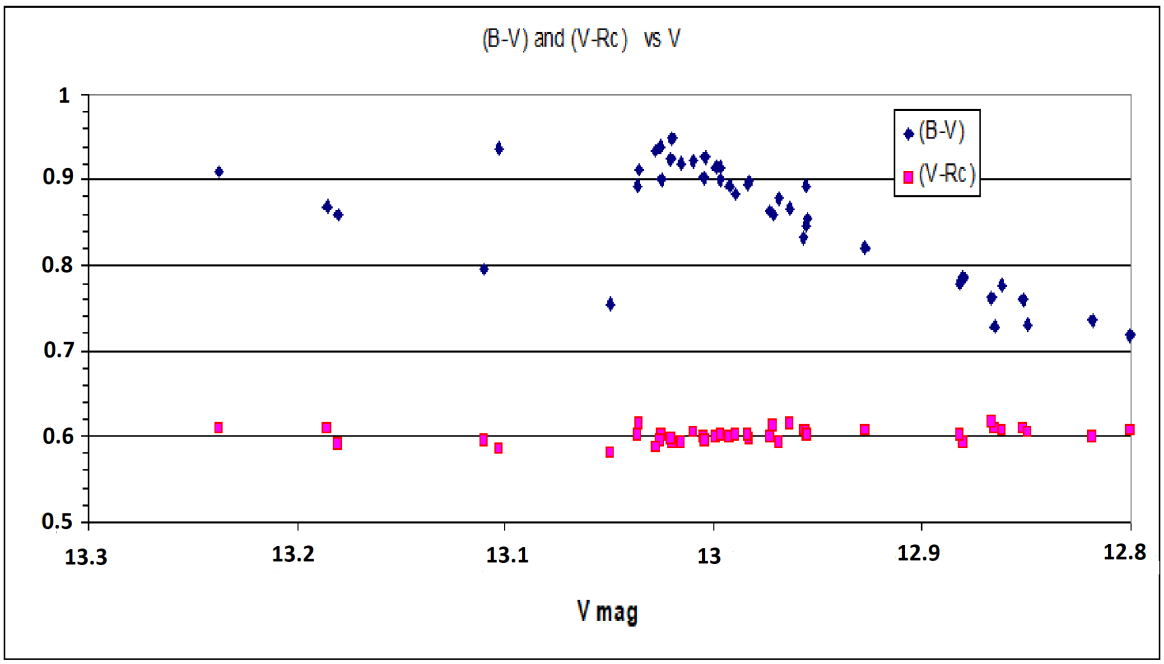


Figure 2. Color-magnitude relations demonstrating the "bluer when brighter" effect in the NGC 3516.

The spectra of NGC 3516 in the spectral range λ4000 Å to λ7000 Å are presented in arbitrary units and shifted along the Y-axis for profile comparison (Figure 3). It was noted that on 22 May 2020, the spectrum presents prominent narrow resolved emission lines [FeVII] 5721 Å, 6087 Å. These coronal emission lines probably originate from the inner region, and for their creation, most likely a hot X-ray wind is needed [25–27].

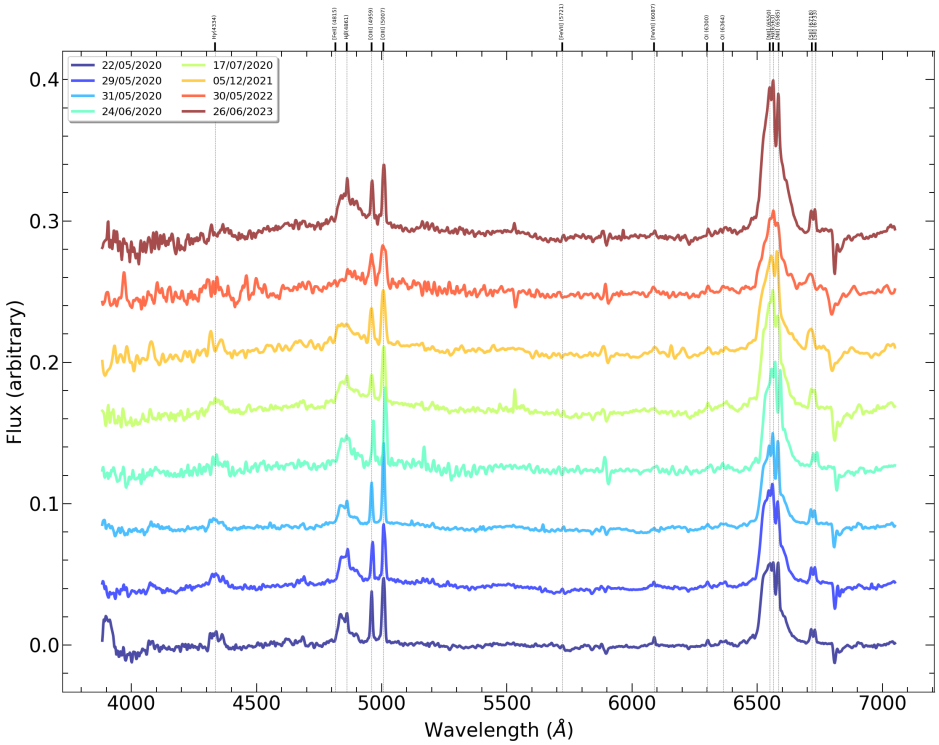


Figure 3. Spectra of NGC 3516, in the spectral range from λ4000 Å to λ7000 Å during the period of 2020–2023. Spectra are normalized to the mean F[OIII] for comparison and are shifted along the Y-axis.

Table 2 includes data such as continuum fluxes, emission line fluxes and equivalent widths. The [SII] flux in Table 2 refers to the combined flux of the [SII] doublet lines at λ6717 Å and λ6731 Å.

Table 2. Fluxes in the emission lines and continuum in the spectrum of NGC 3516.

Date	Line [1]	$F_{\lambda}^{Cont.}$ erg cm^{-2} s^{-1} Å^{-1}	F_{λ}^{line} erg cm^{-2} s^{-1}	$\sigma F_{\lambda}^{line}$ erg cm^{-2} s^{-1}	EQW Å	FWHM [2] Å
20 April 2020	Hβ	4.34×10^{-14}	2.48×10^{-13}	5.62×10^{-15}	6 ± 0.13	41
	[OIII]	4.12×10^{-14}	3.93×10^{-13}	1.62×10^{-14}	10 ± 0.39	23
	[OIII]	4.04×10^{-14}	9.57×10^{-13}	4.37×10^{-14}	24 ± 1.08	20
	Hα+[NII]	4.31×10^{-14}	2.16×10^{-12}	2.79×10^{-14}	50 ± 0.64	73
	[SII]	4.19×10^{-14}	2.36×10^{-13}	8.75×10^{-15}	6 ± 0.21	25
22 May 2020	Hγ	3.53×10^{-14}	4.44×10^{-13}	6.67×10^{-15}	13 ± 0.19	62
	Hβ	3.46×10^{-14}	7.65×10^{-13}	9.91×10^{-15}	22 ± 0.29	72
	[OIII]	3.42×10^{-14}	1.81×10^{-13}	1.70×10^{-14}	5 ± 0.50	10
	[OIII]	3.248×10^{-14}	2.98×10^{-13}	2.32×10^{-14}	9 ± 0.72	12
	[FeVII]	2.77×10^{-14}	2.20×10^{-14}	2.61×10^{-15}	0.79 ± 0.09	8
	Hα+[NII]	2.66×10^{-14}	2.41×10^{-12}	2.75×10^{-14}	91 ± 1.04	82
	[SII]	2.56×10^{-14}	1.09×10^{-13}	3.79×10^{-15}	4 ± 0.14	27
29 May 2020	Hγ	2.01×10^{-14}	2.20×10^{-13}	3.63×10^{-15}	11 ± 0.18	57
	Hβ	2.05×10^{-14}	4.61×10^{-13}	5.63×10^{-15}	22 ± 0.27	77
	[OIII]	1.99×10^{-14}	1.14×10^{-13}	8.70×10^{-15}	6 ± 0.44	13
	[OIII]	1.97×10^{-14}	1.36×10^{-13}	1.15×10^{-14}	7 ± 0.58	11
	[FeVII]	1.73×10^{-14}	2.89×10^{-14}	9.17×10^{-16}	1.67 ± 0.05	29
	Hα+[NII]	1.76×10^{-14}	1.84×10^{-12}	2.08×10^{-14}	105 ± 1.19	83
	[SII]	1.75×10^{-14}	8.08×10^{-14}	2.44×10^{-15}	5 ± 0.14	31
31 May 2020	Hγ	2.73×10^{-14}	3.33×10^{-13}	4.65×10^{-15}	12 ± 0.17	67
	Hβ	3.28×10^{-14}	6.02×10^{-13}	7.32×10^{-15}	18 ± 0.22	77
	[OIII]	3.23×10^{-14}	1.71×10^{-13}	1.58×10^{-14}	5 ± 0.48	10
	[OIII]	3.07×10^{-14}	3.31×10^{-13}	3.16×10^{-14}	11 ± 1.03	10
	[FeVII]	2.97×10^{-14}	2.82×10^{-14}	1.16×10^{-15}	0.95 ± 0.04	23
	Hα+[NII]	2.98×10^{-14}	2.64×10^{-12}	3.04×10^{-14}	88 ± 1.010	82
	[SII]	3.05×10^{-14}	1.21×10^{-13}	4.53×10^{-15}	4 ± 0.15	25
24 June 2020	Hγ	1.41×10^{-14}	2.31×10^{-13}	3.56×10^{-15}	16 ± 0.25	61
	Hβ	1.88×10^{-14}	5.03×10^{-13}	6.34×10^{-15}	27 ± 0.34	75
	[OIII]	1.93×10^{-14}	1.33×10^{-13}	1.22×10^{-14}	7 ± 0.63	10
	[OIII]	1.87×10^{-14}	2.34×10^{-13}	1.82×10^{-14}	13 ± 0.97	12
	[FeVII]	1.96×10^{-14}	1.85×10^{-14}	1.00×10^{-15}	0.95 ± 0.05	17
	Hα+[NII]	1.93×10^{-14}	2.25×10^{-12}	2.58×10^{-14}	116 ± 1.34	82
	[SII]	1.93×10^{-14}	8.88×10^{-14}	3.23×10^{-15}	5 ± 0.17	25
17 July 2020	Hγ	1.72×10^{-14}	1.58×10^{-13}	2.83×10^{-15}	9 ± 0.16	52
	Hβ	2.29×10^{-14}	2.48×10^{-13}	3.11×10^{-15}	11 ± 0.14	75
	[OIII]	2.38×10^{-14}	1.03×10^{-13}	5.14×10^{-15}	4 ± 0.22	19
	[OIII]	2.37×10^{-14}	1.64×10^{-13}	1.13×10^{-14}	7 ± 0.48	14
	Hα+[NII]	2.49×10^{-14}	1.66×10^{-12}	2.07×10^{-14}	67 ± 0.83	75
	[SII]	2.46×10^{-14}	9.86×10^{-14}	3.83×10^{-15}	4 ± 0.16	24
05 Dec. 2021	Hγ	1.74×10^{-14}	1.19×10^{-13}	4.08×10^{-15}	7 ± 0.23	27
	Hβ	1.95×10^{-14}	2.55×10^{-13}	3.20×10^{-15}	13 ± 0.16	75
	[OIII]	1.95×10^{-14}	1.11×10^{-13}	7.00×10^{-15}	6 ± 0.36	15
	[OIII]	1.94×10^{-14}	1.51×10^{-13}	9.94×10^{-15}	8 ± 0.51	14
	Hα+[NII]	2.12×10^{-14}	1.47×10^{-12}	1.71×10^{-14}	69 ± 0.81	80
	[SII]	2.10×10^{-14}	1.01×10^{-13}	4.06×10^{-15}	5 ± 0.19	23
30 May 2022	Hβ	2.61×10^{-14}	1.88×10^{-13}	1.41×10^{-15}	7 ± 0.05	124
	[OIII]	2.61×10^{-14}	1.22×10^{-13}	5.93×10^{-15}	5 ± 0.22	19
	[OIII]	2.58×10^{-14}	1.72×10^{-13}	7.58×10^{-15}	7 ± 0.29	21
	Hα+[NII]	2.60×10^{-14}	1.15×10^{-12}	1.43×10^{-14}	44 ± 0.55	76
	[SII]	2.55×10^{-14}	7.29×10^{-14}	2.81×10^{-15}	3 ± 0.11	24
26 June 2023	Hβ	1.81×10^{-14}	2.78×10^{-13}	3.19×10^{-15}	15 ± 0.18	82
	[OIII]	1.87×10^{-14}	7.62×10^{-14}	6.52×10^{-15}	4 ± 0.35	11
	[OIII]	1.81×10^{-14}	1.26×10^{-13}	9.94×10^{-15}	7 ± 0.55	12
	Hα+[NII]	1.99×10^{-14}	2.05×10^{-12}	2.11×10^{-14}	103 ± 1.06	91
	[SII]	1.99×10^{-14}	8.01×10^{-14}	2.66×10^{-15}	4 ± 0.13	28

[1] Central wavelengths: Hγ 4340 Å, Hβ 4861 Å, [OIII] 4959 Å and 5007 Å, [FeVII] 6086 Å, Hα+[NII] 6562 Å, [SII] 6730 Å. [2] Uncertainty in FWHM is $\pm$0.94 Å.

We added the transmission curves of the *B*, *V* and *Rc* photometric filters over the spectrum of NGC 3516 observed on 5 December 2021, to show which emission lines can affect the brightness of an object in the filters used (see Figure 4). The emission line Hβ 4861 Å falls within the *B* filter range, [OIII] 5007Å within the *V* filter and Hα 6563 Å together with the [SII] 6717 Å , 6731 Å doublet within the *Rc* filter range.

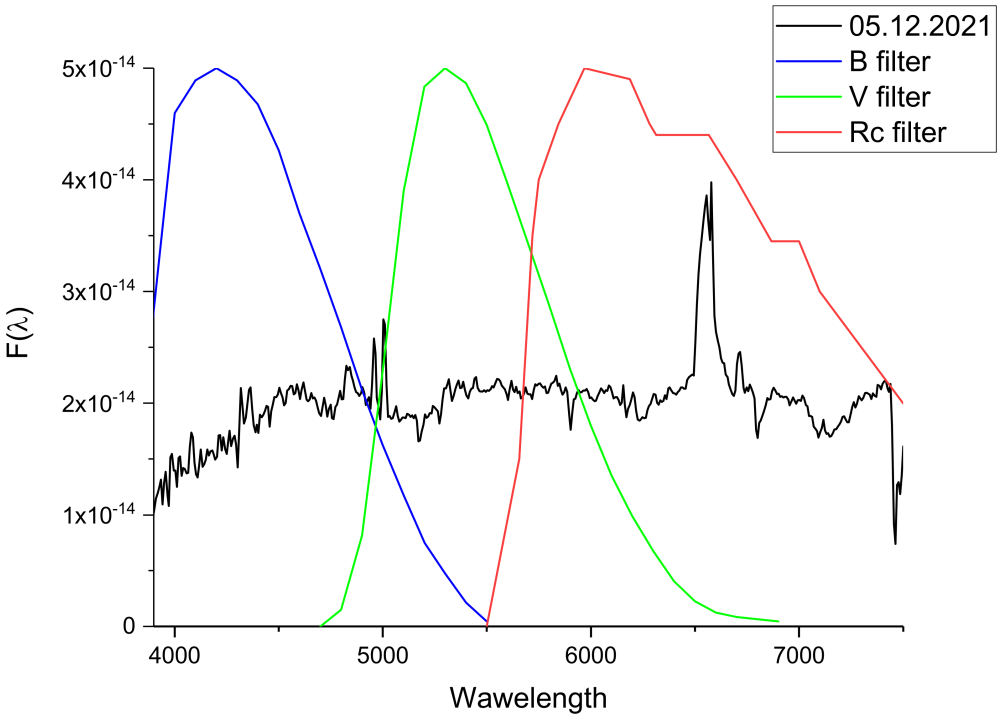


Figure 4. Overlay of *B*, *V* and *Rc* filters on the spectrum from 5 December 2021.

We have visualized the change in the fluxes of the Hα+[NII] and Hβ lines in Figure 5, which allows us to trace their variations over time.

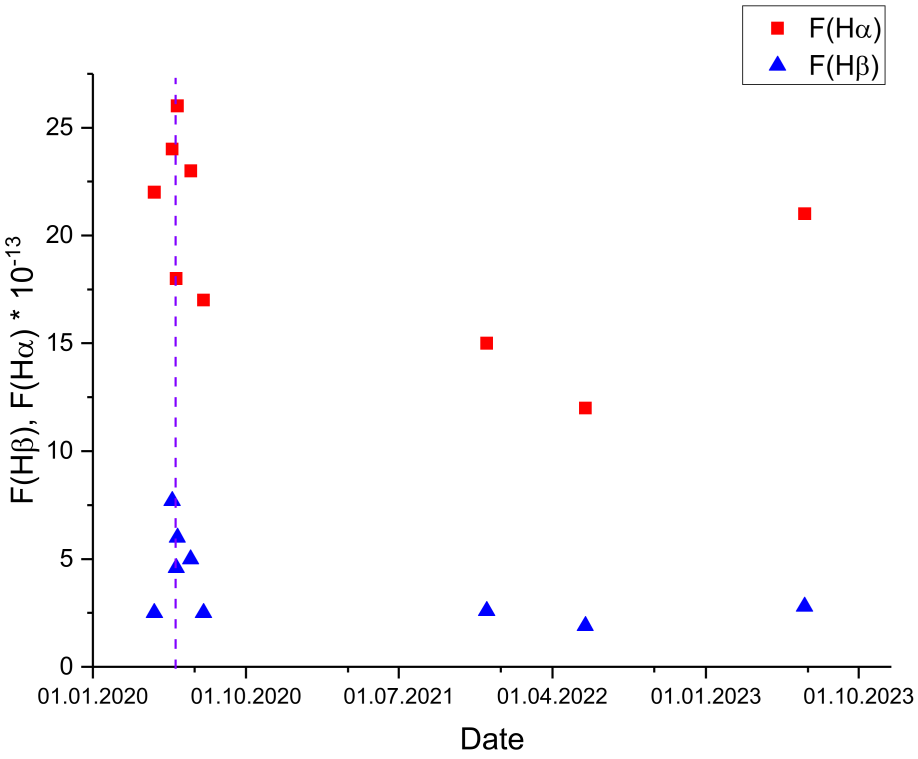


Figure 5. The change in the fluxes of the Hα+[NII] and Hβ lines. The vertical dashed line corresponds to the maximum of the X-ray flash from [6].

The Spectral Energy Distribution (SED) of the galaxy in the long-wavelength range is constructed based on continuum fluxes. Figure 6 demonstrates that the enhancement of

optical continuum observed in 2020 corresponds to an increase in the ionizing radiation in the short-wavelength region of the spectrum.

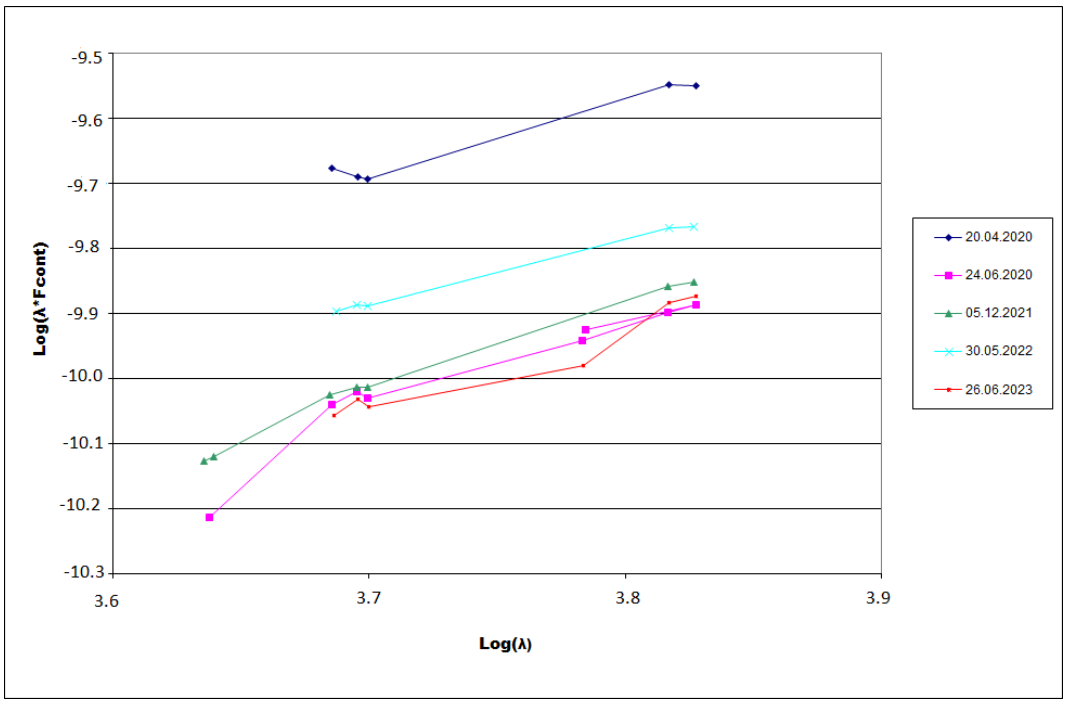


Figure 6. SED of the galaxy NGC 3516 in the long-wavelength range, based on continuum fluxes.

The SED at high continuum brightness corresponds to the maximum values of fluxes in the Hβ and Hα lines. Two points on the light curve related to 2022 (Figure 1) correspond to a slight increase in the continuum level (Table 2) and a "rise" in the SED (Figure 6). At the same time, the emission fluxes in the Hβ and Hα lines remain at a low level, which leads to a decrease in their equivalent widths. The galaxy's brightness reaches another maximum in 2024, an increase in emission fluxes is observed in mid-2023, the SED is at a low level, but its slope changes and the color indices decrease.

For a quantitative assessment of the broad-line region (BLR) size at different epochs, we calculated the continuum luminosity at λ5100 Å (L5100), adopting a luminosity distance to NGC 3516 of $D_L = 38$ Mpc, and applied the empirical R$\check{}$L relation from Bentz et al. [28]. The results are summarized in Table 3. The characteristic size of the BLR varies between approximately 0.13 and 0.20 light-days across different observational epochs. The largest value was obtained in April 2020 (0.20 light-days), corresponding to the period of enhanced continuum luminosity. A slight increase in R is observed again in 2023, which matches a higher (though not maximum) SED position in Figure 6. By June 2023, a gradual decrease in $R_{\rm BLR}$ to 0.13 light-days is observed, corresponding to a decline in continuum flux and the evolution of the spectral energy distribution.

The spectrum of NGC 3516 obtained on 20 April 2020, with the "West" 1-meter (TSHAO) telescope was employed to separate the complex line profiles into individual components. When approximating emission line profiles in the spectrum with composite models, we apply a so-called "uninformative" approach as prior information for each model parameter. In this approach, the probability of a given parameter value is uniformly distributed within a specific range derived, for example, from previous studies of this object.

To describe the stellar component of the galaxy, we approximate the combined (stitched) spectrum of the galaxy using a set of templates with metallicity $[\frac{Fe}{H}] = [-0.4, 0.0, +0.22]$ and ages of $[7.94, 10.0, 12.6]$ Gy, a total of 9 spectra. In other words, we use a combination of

spectra to accurately describe the light emitted by all the stars in the galaxy and account for their contribution to the overall spectrum. The result is shown in Figure 7 [29].

Table 3. Flux, luminosity and BLR size estimates for NGC 3516.

Epoch Date	$F_{5100\,\text{Å}}$ erg cm^{-2} s^{-1} Å^{-1}	L_{5100} erg s^{-1}	R_{BLR} Light-Days
20 April 2020	4.04×10^{-14}	6.97×10^{39}	0.20
22 May 2020	3.24×10^{-14}	5.59×10^{39}	0.18
29 May 2020	1.90×10^{-14}	3.40×10^{39}	0.14
31 May 2020	2.92×10^{-14}	5.05×10^{39}	0.18
24 June 2020	1.87×10^{-14}	3.22×10^{39}	0.14
17 July 2020	2.37×10^{-14}	4.10×10^{39}	0.15
05 Dec. 2021	1.94×10^{-14}	3.35×10^{39}	0.14
30 May 2022	2.58×10^{-14}	4.46×10^{39}	0.16
26 June 2023	1.81×10^{-14}	3.13×10^{39}	0.13

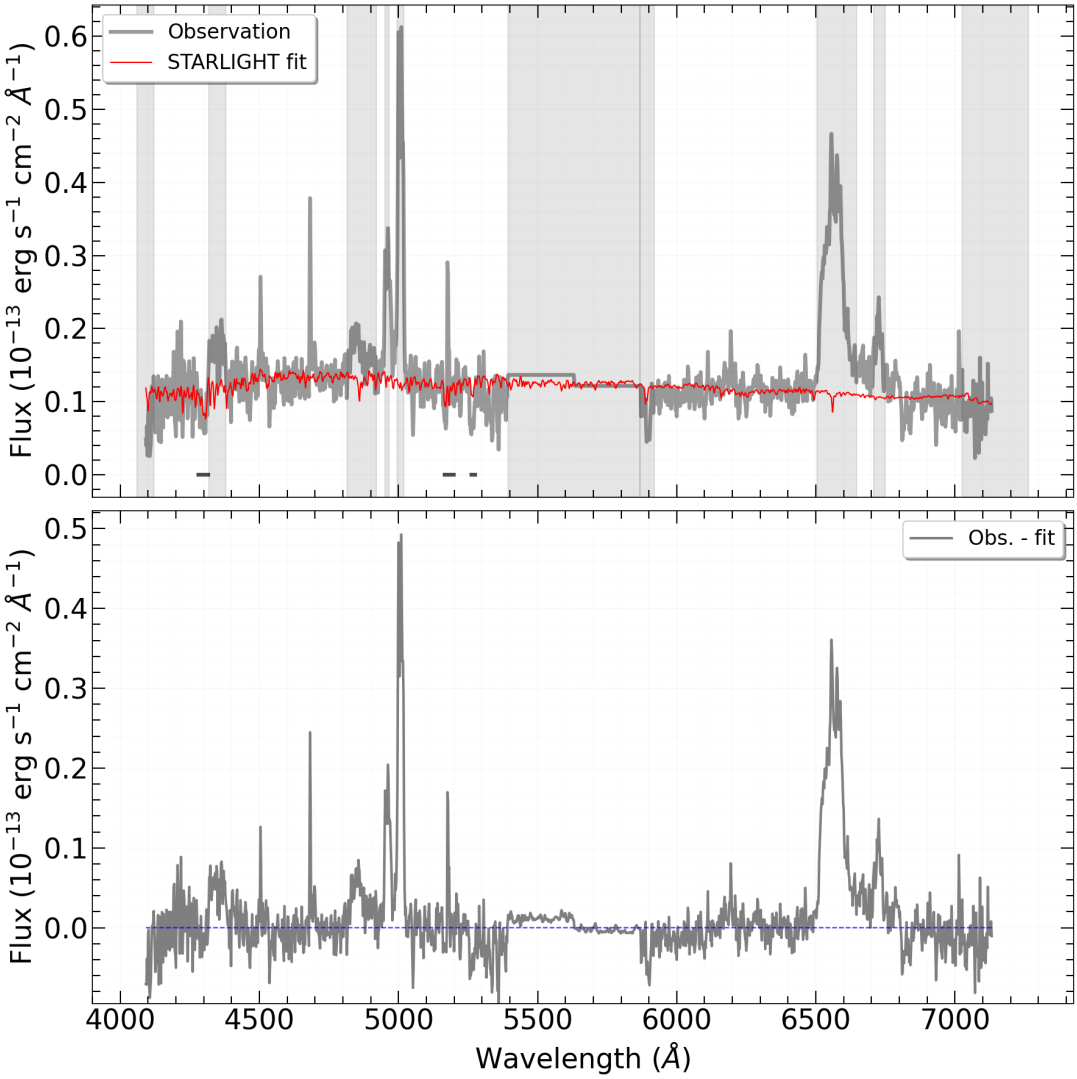


Figure 7. Result of considering the stellar component in the spectrum of the galaxy NGC 3516 using the `STARLIGHT` [29] package (https://starlightsoftware.github.io/, accessed on 6 November 2024) for observations dated 20 April 2020.

We apply a Bayesian approach to determining the main parameters in the region of narrow line emission (NLE) and broad line emission (BLE), such as velocity dispersion and radial velocities, and identifying the most plausible model (the number of components in BLE). The "Bayesian evidence" factor is determined using the nested sampling method implemented in the `DYNESTY` package (Appendix A).

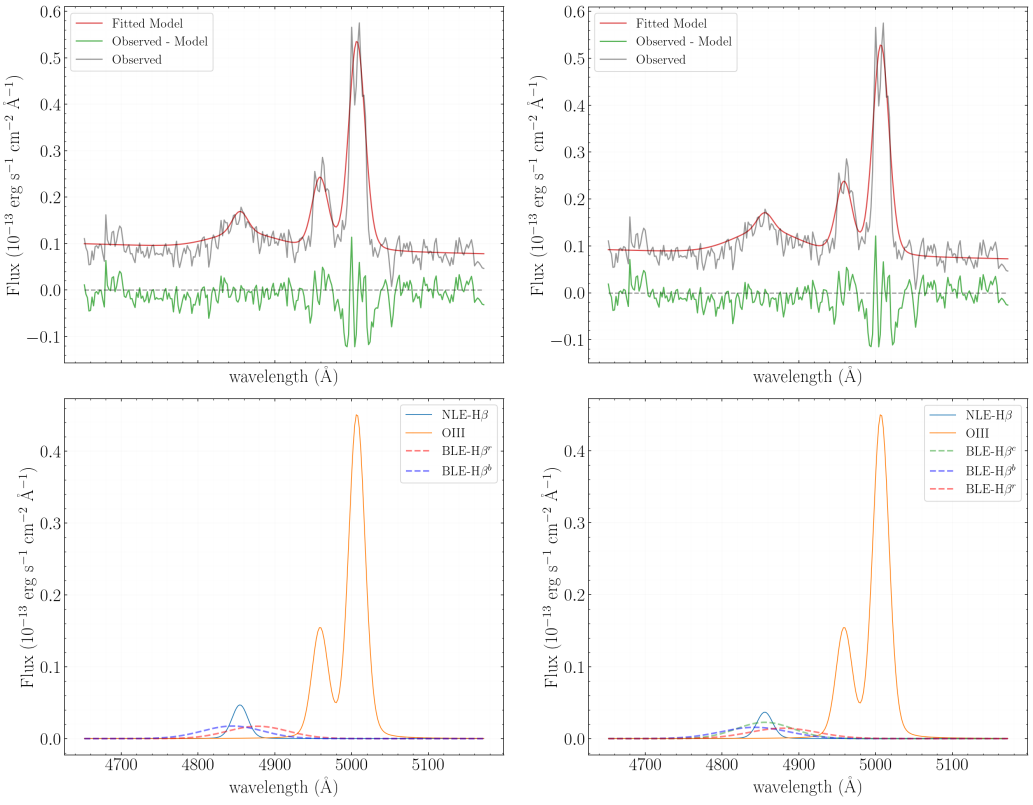
3.2. Spectral Modeling

Spectral Range λ4652 Å–λ5172 Å

In this spectral range, NLE are represented by Hβ 4861 Å, [OIII] 4959 Å and [OIII] 5007 Å. The NLE profiles are described using a Voigt function, assuming the same velocity dispersion for all lines. The amplitude ratio for the [OIII] doublet is fixed at 1:2.98. A two-component profile is used for BLE in Hβ. A total of 12 parameters were used in the model. The results are shown in Figure 8.

Spectral Range λ6192 Å–λ6894 Å

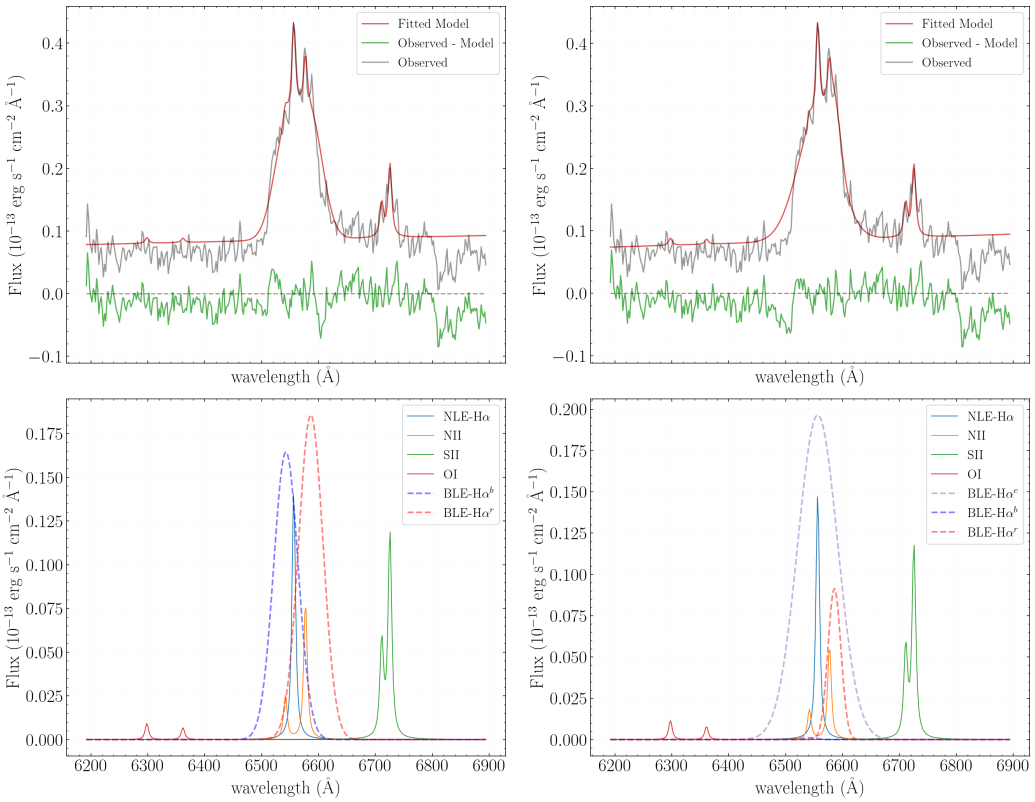
In this spectral range, the NLEs include the following: [OI] 6300.3 Å, [OI] 6363.8 Å, Hα 6564.6 Å, [NII] 6549.9 Å, 6585.3 Å and [SII] 6718.3 Å, 6732.7 Å, Figure 8. The NLE lines are modeled using a `Voigt` function [30] with identical velocity dispersions. The amplitude ratio for the [NII] doublet is set at 1:3.05. As a result of model fitting we estimated FWHM (Hα_{BC}) = 3747^{+98}_{-92} km s^{-1}, FWHM (Hα_{NC}) = 353^{+23}_{-15} km s^{-1}, EW (Hα_{NC}) = 28 Å.



(**a**) Hβ, two-component model

(**c**) Hβ, three-component model

Figure 8. *Cont.*



(**b**) Hα, two-component model (**d**) Hα, three-component model

Figure 8. The result of the approximation with the combined profile.

For the Hα range, the three-component model is preferred over the two-component model for describing the BLE profile, as $\ln B_{0,1} = -2.8$, indicating that the three-component model is 16 times more likely than the two-component one. For the Hβ range, the two- and three-component models exhibit similar statistical significance ($\ln B_{0,1} = 0.9$). The three-component model was chosen for consistency, considering the noise level and uncertainties. All approximations for the NLE lines used a Voigt profile, while the BLE lines were modeled with either a two- or three-component Gauss profile. The high noise level in this region prevents us from having a precise measurement of $H\beta_{BC}$ velocity dispersion $\sigma_{\texttt{line}}$ used for Black Hole mass estimation.

4. Discussion

The main goal of our work was to study the photometric and spectral variability of the Seyfert galaxy NGC 3516. We obtained brightness estimates in the *B*, *V* and *Rc* filters, as well as flux measurements of all observed emission lines and the continuum near these lines.

Figure 1 shows the light curves of NGC 3516 in the *B*, *V* and *Rc* filters based on observational data collected from 2014 to 2025 and supplemented by results from [2,6]. Our brightness values in the *V* and *Rc* filters are approximately 0.2 mag higher than those reported in [2]; the cause of this discrepancy remains unclear. In the *B* filter, the values from [6] lie slightly above our light curve, while those from [2] lie somewhat below it. Overall, the agreement in the *B* filter can be considered satisfactory, and we will rely primarily on these data in the following discussion.

Thus, Figure 1 shows brightness maxima in 2014 and 2016. A subsequent brightening was observed in 2019. A powerful X-ray flare on 1 April 2020, caused an increase in optical brightness by about 0.2 mag, which was significantly weaker than the 2016 maximum. A

new rise followed the subsequent decline in brightness in 2021. Due to the irregular nature of our observations, we can only note a general trend of gradual brightening from 2021 to 2025, without discussing the details of the process. In 2025, the B magnitude reached the same peak value as observed in 2016.

Maximum fluxes in the emission lines Hβ, Hα and in the continuum were recorded in spring 2020. About 3–4 months later, these values decreased by approximately a factor of two and remained low until 2023, when an increase began. Given the lack of data between June 2022 and January 2023, it is possible that the rise in emission fluxes started earlier.

During the active phase (April–May 2020), emission lines of [FeVII] λ6087Å appeared in the galaxy's spectrum. The mechanisms of coronal line formation and the sources of their origin are discussed in several works, e.g., [26,27,31]. The formation of coronal lines may indicate a hardening of the SED in the X-ray region. A Tidal Disruption Event or an Extreme Coronal Line Emission may also explain the sudden appearance of coronal lines. Another possibility is the weakening of the central continuum, allowing the observation of weak emission lines like [FeVII] [27].

The black hole mass was estimated using the formulas from Greene [32]. A moderate-resolution spectrum obtained on 20 April 2020, was used, in which the broad components of the hydrogen lines were identified. Based on the luminosity and FWHM of the broad components of the Hα and Hβ lines, we obtained estimates of the black hole mass: $M_{\rm BH} \approx (2.28 \pm 0.8) \times 10^7\ M_\odot$, $M_{\rm BH} \approx (1.36 \pm 1.0) \times 10^7\ M_\odot$, respectively. This is in agreement with the estimation by other authors [33,34]. The uncertainties in the derived values are mainly due to the low intensity of the broad components.

Despite the rather large volume of photometric data, the low cadence does not allow obtaining accurate estimates of time delays. Comparison of the curves obtained in the B and V filters gives Lag values of about zero for the periods 2014–2019 and 2020–2025.

It is worth mentioning that this study presents the selection of models solely within the framework of debating the criteria for model selection. In the cases of noisy data and potentially the presence of instrumental noise, reliance solely on residual quality may result in inaccurate interpretations. We propose the utilization of the Bayesian factor as a model selection criterion. The findings demonstrate its efficacy in discerning suitable models where residual quality alone may prove inadequate.

5. Conclusions

This paper presents the results of new spectral and photometric observations of NGC 3516, performed with the FAI and ShAO telescopes in 2020–2023 and 2014–2025, respectively. The photometric data cover the brightness increases of the galaxy in 2016 and 2019–2020. A new active phase began in 2021, and at the end of our observations in 2025, the brightness of the galaxy reached the values recorded during the outburst of 2016. Analysis of our data and the results of other observations showed that the color index $(B - V)$ decreases with increasing brightness; i.e., the brighter the galaxy, the bluer it is.

The fluxes in specific lines and the optical continuum had maximum values in 2020, shortly after the X-ray flash. The next increase in emission fluxes was recorded in mid-2023. The main interest of spectral studies is the characteristics of the broad components of the emission lines and their variation. The procedure for separating the hydrogen line profiles into components was performed only for one spectrum from 20 April 2020. (The rest spectra were obtained with low dispersion). Model calculations were carried out to approximate the profiles of the broad components Hα and Hβ; variants of 2- and 3-component systems were considered.

In the future, we plan to conduct spectral and photometric observations synchronously and to obtain spectra with better spectral resolution for a detailed study of the broad

components of hydrogen lines. This will allow us to determine the sizes of BLR zones and to study their changes.

Author Contributions: Conceptualization, methodology and visualization, S.S. and A.S.; software, A.S.; validation, L.A.; formal analysis, L.K. and Y.A.; investigation, S.S. and L.K.; resources, V.K., N.H. and S.R.; data curation, S.S. and L.A.; writing—original draft preparation, review and editing, S.S., A.S. and L.K.; supervision, project administration and funding acquisition, S.S. All authors have read and agreed to the published version of the manuscript.

Funding: This research is funded by the Ministry of Science and Higher Education of the Republic of Kazakhstan (Grant No. AP22784884 and Grant No. BR24992759).

Informed Consent Statement: Not applicable.

Data Availability Statement: Research data can be provided upon reasonable request.

Acknowledgments: The authors express their gratitude to the SHAO team and the FAI observers for their assistance in organizing and conducting the spectral and photometric observations.

Conflicts of Interest: The authors declare no conflicts of interest. The funders had no role in the design of the study, in the collection, analyses or interpretation of data, in the writing of the manuscript or in the decision to publish the results.

Appendix A. Theoretical Background for Bayesian Analysis

Recall that the task in the Bayesian approach is formulated as follows. Given observational data (D) and a model with free parameters (θ), Bayes' theorem is stated as:

$$P(\theta|D) = \frac{P(D|\theta)P(\theta)}{P(D)}, \tag{A1}$$

where the likelihood function $P(D|\theta)$ is determined by the observed data, and the prior information about the parameters and what we already know about the model's parameters is given by the probability distribution function $P(\theta)$. Often, $P(\theta)$ is specified as a uniform distribution over a specific range of values, though in some cases, it is set as a normal distribution centered around a most likely value.

The greatest difficulty in obtaining absolute values of $P(D|\theta)$ comes from the parameter $P(D)$, Bayesian evidence, which defines the probability distribution of obtaining the observed data across the entire parameter space θ, which is

$$Z = P(D) = \int_{R^N} P(D|\theta)P(\theta)d\theta, \tag{A2}$$

which is often not possible. In the case where $P(\theta)$ is specified as a uniform distribution over the entire parameter space and we assume that $P(D) = 1$, we obtain

$$P(\theta|D) = P(D|\theta), \tag{A3}$$

which automatically leads us to the standard least squares method if the likelihood function is a normal distribution.

The selection of the most "plausible" model between model 0 and model 1 is based on the Bayesian factor:

$$B_{0.1} = Z_0/Z_1, \tag{A4}$$

or, equivalently:

$$\ln B_{0.1} = \ln Z_0 - \ln Z_1. \tag{A5}$$

There is a Jeffreys scale on which the preference for one model (0) over another (1) is evaluated. It is generally accepted that if $\ln B_{0.1} < 1$, the decision is inconclusive, and the models are essentially equivalent. If $\ln B_{0.1} = \{1-2.5\}$, there is significant preference for model 0; if $\ln B_{0.1} = \{2.5-5\}$ model 0 is clearly preferable to model 1; and if $\ln B_{0.1} > 5$, model 0 should definitely be chosen as the priority over model 1.

Note

[1] https://ned.ipac.caltech.edu (Access date: 6 November 2024).

References

1. Andrillat, Y.; Souffrin, S. Variations du Spectre du Noyau de la Galaxie de Seyfert NGC 3516. *Astrophys. Lett.* **1968** , *1*, 111–119.
2. Shapovalova, A.I.; Popovic, L.C.; Afanasiev, V.L.; Ilic, D.; Kovacevic, A.; Burenko, A.N.; Chavushyan, V.H.; Marčeta-Mandić, S.; Spiridonova, O.; Valdes, J.R.; et al. Long-term optical spectral monitoring of a changing-look active galactic nucleus NGC 3516—I. Continuum and broad-line flux variability. *Mon. Not. R. Astron. Soc.* **2014**, *485*, 4790–4803. [CrossRef]
3. Cherepashchuk, A.M.; Lyutyi, V.M. Rapid Variations of Halpha Intensity in the Nuclei of Seyfert Galaxies NGC 4151, 3516, 1068. *Astrophys. Lett.* **1973**, *13*, 165.
4. De Rosa, G.; Fausnaugh, M.M.; Grier, C.J.; Peterson, B.M.; Denney, K.D.; Horne, K.; Bentz, M.C.; Ciroi, S.; Dalla Bontà, E.; Joner, M.D.; et al. Velocity-resolved Reverberation Mapping of Five Bright Seyfert 1 Galaxies. *ApJ* **2018**, *866*, 133. [CrossRef]
5. Denney, K.D.; Peterson, B.M.; Pogge, R.W.; Adair, A.; Atlee, D.W.; Au-Yong, K.; Bentz, M.C.; Bird, J.C.; Brokofsky, D.J.; Chisholm, E.; et al. Diverse Kinematic Signatures from Reverberation Mapping of the Broad-Line Region in AGNs. *Astrophys. J.* **2009**, *704*. [CrossRef]
6. Ilic, D.; Oknyansky, V.; Popovic, L.; Tsygankov, S.; Belinski, A.; Tatarnikov, A.M.; Dodin, A.V.; Shatsky, N.I.; Ikonnikova, N.P.; Rakić, N.; et al. A flare in the optical spotted in the changing-look Seyfert NGC 3516. *Astron. Astrophys.* **2020**, *638*, 7. [CrossRef]
7. Popovic, L.; Ilic, D.; Burenkov, A.; Alvarez, V.M.P.; Marčeta-Mandić, S.; Kovačević-Dojčinović, J.; Shablovinskaya, E.; Kovačević, A.B.; Marziani, P.; Chavushyan, V.; et al. Long-term optical spectral monitoring of a changing-look active galactic nucleus NGC 3516. II. *Astron. Astrophys.* **2020**, *675*, 14. [CrossRef]
8. Kraemer, S.B.; Crenshaw, D.M.; George, I.M.; Netzer, H.; Turner, T.J.; Gabel, J.R. Variable Ultraviolet Absorption in the Seyfert 1 Galaxy NGC 3516: The Case for Associated Ultraviolet and X-Ray Absorption. *Astrophys. J.* **2002**, *577*, 98. [CrossRef]
9. Mathur, S.; Wilkes, B.J.; Aldcroft, T. The X-Ray Warm Absorber in NGC 3516. *Astrophys. J.* **1997**, *478*, 182. [CrossRef]
10. Turner, T.J.; Kraemer, S.B.; George, I.M.; Reeves, J.N.; Bottorff, M.C. Complex X-Ray Absorption and the Fe Kα Profile in NGC 3516. *Astrophys. J.* **2005**, *618*, 155. [CrossRef]
11. Ilić, D.; Popović, L.; Burenkov, A.; Shablovinskaya, E.M.E.U.R.; Moiseev, A.; Oparin, D.; Patiño Álvarez, V.; Chavushyan, V.; Marziani, P. Long-Term Optical Monitoring of Broad-Line AGNs (LoTerm AGN): Case Study of NGC 3516. *Physics* **2024**, *6*, 3. [CrossRef]
12. Blandford, R.D.; McKee, C.F. Reverberation mapping of the emission line regions of Seyfert galaxies and quasars. *Astrophys. J.* **1982**, *255*, 419–439. [CrossRef]
13. Urry, C.M.; Padovani, P. Unified Schemes for Radio-Loud Active Galactic Nuclei. *Astron. Soc. Pac.* **1995**, *107*, 803. [CrossRef]
14. Mehdipour, M.; Kriss, G.A.; Brenneman, L.W.; Costantini, E.; Kaastra, J.S.; Branduardi-Raymont, G.; Di Gesu, L.; Ebrero, J.; Mao, J. Changing-look Event in NGC 3516: Continuum or Obscuration Variability? *Astrophys. J.* **2022**, *925*, 84. [CrossRef]
15. Astronomical Imaging Software. Available online: https://diffractionlimited.com/product/maxim-dl/ (accessed on 6 November 2024).
16. Doroshenko, V.; Sergeev, S.; Merkulova, N.I.; Sergeeva, E.A.; Golubinsky, Y.V.; Pronik, V.I. BVRI CCD Photometry of Comparison Stars in the Fields of 44 Active Galaxies. *Astron. Soc. Pac.* **2007**, *360*, 69.
17. Shomshekova, S.A.; Reva, I.V.; Kondratyeva, L. Standardization of the photometric system of the 1-meter telescope on TSHAO. *Natl. Acad. Sci. Repub. Kazakhstan-Phys.-Math. Ser.* **2017**, *4, 155–161*.
18. Fitzpatrick, M.; Placco, V.; Bolton, A.; Merino, B.; Ridgway, S.; Stanghellini, L. Modernizing IRAF to Support Gemini Data Reduction. *arXiv* **2024**, arXiv:2401.01982. [CrossRef]
19. Kharitonov, A.V.; Tereshchenko, V.; Knyazeva, L.N. *Spectrophotometric Catalog of Stars*, 3rd ed.; Kazakh University: Kazakhstan, Almaty, 2011; ISBN 9965-29-626-X.
20. Schlafly, E.F.; Finkbeiner, D.P. Measuring Reddening with Sloan Digital Sky Survey Stellar Spectra and Recalibrating Sfd. *Astrophys. J.* **2011**, *737*, 103. [CrossRef]
21. Speagle, J. Dynesty: A dynamic nested sampling package for estimating Bayesian posteriors and evidences. *Mon. Not. R. Astron. Soc.* **2020**, *493*, 3132–3158. [CrossRef]

22. Koposov, S.; Speagle, J.; Barbary, K.; Ashton, G.; Bennett, E.; Buchner, J.; Scheffler, C.; Cook, B.; Talbot, C.; Guillochon, J.; et al. DYNESTY. 2023. Available online: https://zenodo.org/records/8408702 (accessed on 6 November 2024).
23. Oknyansky, V.; Mikailov, K.; Huseynov, N. Changing Looks of the Nucleus of Seyfert Galaxy NGC 3516 during 2016–2020. *Astron. Rep.* **2020**, *64*, 979–984. [CrossRef]
24. Oknyansky, V.L.; Brotherton, M.S.; Tsygankov, S.S.; Dodin, A.V.; Bao, D.W.; Zhao, B.X.; Du, P.; Burlak, M.A.; Ikonnikova, N.P.; Tatarnikov, A.M.; et al. Multi-Wavelength Monitoring and Reverberation Mapping of a Changing Look Event in the Seyfert Galaxy NGC 3516. *Mon. Not. R. Astron. Soc.* **2021**, *505*, 1029–1045. [CrossRef]
25. Cann, J.M.; Satyapal, S.; Abel, N.P.; Ricci, C.; Secrest, N.J.; Blecha, L.; Gliozzi, M. The Hunt for Intermediate-mass Black Holes in the JWST Era. *Astrophys. J.* **2018**, *861*, 142. [CrossRef]
26. Rodriguez-Ardila, A.; May, D.; Panda, S.; Fonseca-Faria, M.A.; Fraga, L. The narrow-line region properties of ESO 138-G001 unveiled by SOAR/SIFS observations. *Mon. Not. R. Astron. Soc.* **2024**, *527*, 10649–10667. [CrossRef]
27. Callow, J.; Graur, O.; Clark, P.; Palmese, A.; Aguilar, J.; Ahlen, S.; BenZvi, S.; Brooks, D.; Claybaugh, T.; Macorra, A.d.; et al. The rate of extreme coronal line emitting galaxies in the Sloan Digital Sky Survey and their relation to tidal disruption events. *Mon. Not. R. Astron. Soc.* **2024**, *535*, 1095–1122. [CrossRef]
28. Bentz, M.C.; Denney, K.D.; Grier, C.J.; Barth, A.J.; Peterson, B.M.; Vestergaard, M.; Bennert, V.N.; Canalizo, G.; Rosa, G.D.; Filippenko, A.V.; et al. The low-luminosity end of the radius-luminosity relationship for active galactic nuclei. *Astrophys. J.* **2013**, *767*, 149. [CrossRef]
29. Cid Fernandes, R.; Mateus, A.; Sodré, L.; Stasińska, G.; Gomes, J.M. Semi-empirical analysis of Sloan Digital Sky Survey galaxies—I. Spectral synthesis method. *Mon. Not. R. Astron. Soc.* **2005**, *358*, 363–378. [CrossRef]
30. Lusso, E.; Fotopoulou, S.; Selwood, M.; Allevato, V.; Calderone, G.; Mancini, C.; Mignoli, M.; Scodeggio, M.; Bisigello, L.; Feltre, A.; et al. Euclid preparation—XXXVIII. Spectroscopy of active galactic nuclei with NISP Euclid Collaboration. *Astron. Astrophys.* **2024**, *685*, A108. [CrossRef]
31. Prieto, A.; Rodriguez-Ardila, A.; Panda, S.; Marinello, M. Erratum: A novel black hole mass scaling relation based on coronal gas, and its dependence with the accretion disc. *Mon. Not. R. Astron. Soc.* **2022**, *511*, 4444–4446. [CrossRef]
32. Greene, J.E.; Ho, L.C. Estimating Black Hole Masses in Active Galaxies Using the H α Emission Line. *Astrophys. J.* **2005**, *630*, 122–129. [CrossRef]
33. Feng, H.C.; Hu, C.; Li, S.S.; Liu, H.T.; Bai, J.M.; Xing, L.F.; Wang, W.Y.; Yang, Z.X.; Xiao, M.; Lu, K.X. Reverberation Mapping of Changing-look Active Galactic Nucleus NGC 3516. *Astrophys. J.* **2021**, *909*, 18. [CrossRef]
34. Koss, M.J.; Ricci, C.; Trakhtenbrot, B.; Oh, K.; den Brok, J.S.; Mejía Restrepo, J.E.; Stern, D.; Privon, G.C.; Treister, E.; Powell, M.C.; et al. BASS. XXII. The BASS DR2 AGN Catalog and Data. *Astrophys. J. Suppl. Ser.* **2022**, *261*, 2. [CrossRef]

Disclaimer/Publisher's Note: The statements, opinions and data contained in all publications are solely those of the individual author(s) and contributor(s) and not of MDPI and/or the editor(s). MDPI and/or the editor(s) disclaim responsibility for any injury to people or property resulting from any ideas, methods, instructions or products referred to in the content.